Photographic response to x-ray irradiation. III: Photographic linearization of beam-foil spectra

C. T. Chantler, J. D. Silver, and D. D. Dietrich

In this paper models for the relation of specular density to incident (x-ray) intensity with uncertainties are applied to experimental data, indicating methods for the correction of additional effects. Linearization and error calculations are simplified by double linear interpolation, and the effect of this is quantified. Relative first-order intensities are determined directly. Secondary linearization or calculation for higher-order lines gives correction factors that yield absolute and relative higher-order intensity ratios. The effects of energy and angle on linearization are included. Densitometry uncertainty is estimated and quantified.

1. Introduction

Models developed in the first two papers[1,2] (denoted herein CI and CII) for smooth-surface, thick emulsions are applied to photographic data collected from two beam-foil spectroscopy experiments. In Table 1 some of the more important parameters referred to in this paper and discussed in the earlier papers are summarized. A dual-arm Johann focusing x-ray spectrometer with curved diffracting crystal focused x rays onto DEF-392 film on the Rowland circle of 150-mm radius (Fig. 1).[3–6] Hydrogenic iron spectral lines in first order (Balmer-β, $\lambda \simeq 7.12$ Å) and fourth-order (Lyman-α, $\lambda \simeq 1.78$ Å) diffraction from PET 002 and ADP 101 crystals are compared. In the second experiment we compare hydrogenic germanium spectra (Balmer-β, $\lambda \simeq 4.64$–4.74 Å; Lyman-α, $\lambda \simeq 1.167$–1.172 Å) similarly, using Si 111 and Si 444 diffracting planes. Secondary peaks in the detection range, of other energies and at different angles, include third-, fourth-, and fifth-order diffraction of Lyman series radiation, first-order diffraction of Balmer series, and heliumlike satellite peaks. This follows earlier research[6,7] in pursuing quantum electrodynamical tests in hydrogenic medium-Z systems. The germanium experiment was reported earlier,[7,8] while new data are presented for hydrogenic iron.

Experimental windows (Section 2) and densitometry arrangements (Sections 3 and 4) affect the conversion of measured densities to source intensities. Problems of fog levels (Section 5) and development procedures (Section 6) are addressed theoretically and with respect to observed data (Section 7). Spectrometer collimation contributes no error in many arrangements, but in the current setup it has some significant well-defined effects, for which allowance may be made (Section 8). Use of nonnormal incident angles and spectral-order overlap can be serious and are discussed in Sections 9, and 10, and 11, respectively. We present linearization of typical spectra with estimated error contributions to illustrate successful implementation and inversion of model formulas for varying energies. A summary of qualitative and quantitative corrections for these effects is given for these experimental energies and angles.

2. Windows

In this and other typical spectrometers, thin 0.0508-mm polypropylene windows with, e.g., 300-nm coatings of aluminum, or 0.0127-mm beryllium windows, are used to cover film holders and reduce stray light, background fogging, and scattered electrons. These windows may lie immediately in front of and parallel to the film. We may allow for this by modifying β, z, and J in Sections 2 and 15 of CI to

$$\beta = [1 - \exp(-\mu_1 d')]\exp[-(\mu_0 t_0 + \mu_w t_w)/\sin\theta]. \quad (1)$$

When this work was performed C. T. Chantler and J. D. Silver were with the Clarendon Laboratory, University of Oxford, Parks Road, Oxford OX1 3PU, England. C. T. Chantler is now with the Quantum Metrology Division, National Institute of Standards and Technology, Gaithersburg, Maryland 20899. D. D. Dietrich is with the Lawrence Livermore National Laboratory, University of California, P.O. Box 808, Livermore, California 94550.

Received 26 November 1991.
0003-6935/93/132411-11$05.00/0.

Table 1. Summary of Primary Variables in CI and CII

Symbol	Definition	Equation/Section CI	CII
$I = I_p/A_d$	Exposing radiation intensity (photons/μm^2)		
D	Specular optical density	Eqs. (6), (25)	Eq. (12)
τ, τ_l	Optical transmission of film or layer	Eq. (3)	Eqs. (9), (11)
T, t_0, t_b	Emulsion, supercoat, and substrate thicknesses	Section 1	Eqs. (1), (6)
M_0	Grains per unit area, monolayer packing density	Eq. (2)	Section 2
$\bar{d}$	Mean AgBr grain diameter in emulsion	Eq. (3)	Section 2
d'	Mean path length through AgBr grain	Eq. (1)	Eq. (1)
μ_0, μ_1, μ'	Attenuation coefficients for gelatin, AgBr, emulsion	Sections (12)–(14)	Eq. (1)
$\sigma_g = \frac{\pi}{4}\bar{d}^2$	Geometric grain cross section	Section 4	Section 2
σ	Effective cross-sectional area per grain	Eq. (1)	Section 2
S	Effective cross section of developed silver cluster	Eq. (3)	Section 2
$C_f = \frac{\sigma}{\sigma_g}, S_f = \frac{S}{\sigma_g}$	Cluster factor, cross-section increase on development	Section 17	Section 2
$\%v/v$	Mean volume fraction of AgBr grains in emulsion	Section 2	Section 2
$V_0 = \frac{4\pi}{3}\bar{d}^3$	Grain volume	Section 3	Section 3
α, d_0, a, b	Semiempirical coefficients of earlier models	Section 2, Eq. (25b)	
J, β, z_m'	Integral and coefficients for absorption of x ray in grain	Eqs. (25), (30)	Section 4
z, z_0, z_j	Exposure probability for depth x, surface or half-layer j		Section 4

3. Oxford Modified Joyce–Loebl Densitometer

Microdensitometry scans the film with a small-angle cone of illuminating light focused at and transmitted through the film. For specular densitometry the transmitted beam is received by a nearly matched aperture of an objective lens, imaged at a fixed slit, and delivered to a photocell. The height and spot size are measured to 10%. The photomultiplier entrance slit width is set to a factor of 2–5 smaller than the illumination source collimation, which is adjustable from >100 to <1 μm. For measurements herein we used a detector slit width of 20 μm on the stage, which was calibrated to 1% by the ratio of photon intensity for this slit versus a 50-μm slit.

The Joyce–Loebl densitometer has longitudinal and transverse drives that are linear and accurate to ~2% but with oscillations of amplitude of ~1.5 μm and a period of 0.9 mm because of the nonuniformity of the drive shaft.[9] This setup was modified so that measurements could be taken at the submicrometer level on longitudinal scans by use of laser interferometry[9,10] or Heidenhain reading.[10,11] A motor was mounted on each of these drives (disconnected from the original drive mechanism) so that automated data collection were permitted.

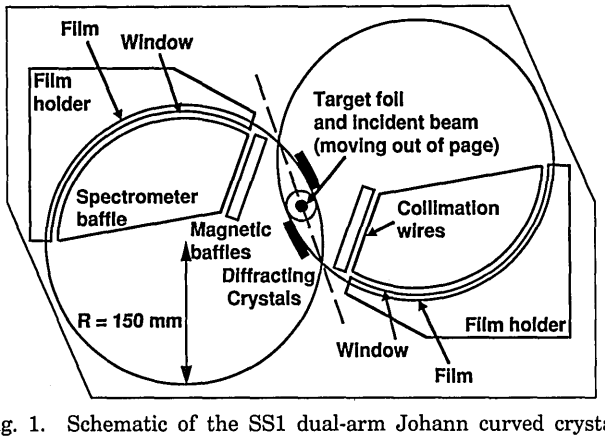

Fig. 1. Schematic of the SS1 dual-arm Johann curved crystal Bragg spectrometer used in the experiments discussed in this paper. The source, diffracting crystal locations, collimating baffles and wires, film holder windows, and film location are illustrated.

A Heidenhain MT101 length gauge (101-mm travel) was added, mounted on a 54-mm Ealing linear stage, so that most regions of the 210-mm active length of the films could be observed and densitized without the films being remounted. Heidenhains have specified accuracies of 1 μm over their full ranges. The transverse drive was connected to a stepping motor controller unit so that full automation for densitometry of each film was permitted, with counterweights balancing the stage. The imbalance of the stage was present in previous densitometry using this instrument but it is likely to have been negligible in most careful short scans. With the counterweights no significant deviation in Heidenhain reading or stepping was observed.

Switching motors on leads to serious (>20-μm) shifts and motion over a period of 20–30 min as the temperature rises, after which a steady state is established. This period was permitted to elapse before any scan was begun. The main additional source of discrepancy was a diurnal temperature variation that had a potential steady linear variation of ~10 μm over several hours or a slow oscillation over a period of a day. Since each scan takes from 40 min to 12 h (depending on the density and the length of each scan), these effects are subsumed within a linear term. In any local (10-mm) region they are negligible.

A serious hysteresis occurs during tracking from the end of one scan to the beginning of another. The Heidenhain reading shifts an amount that is dependent on the program and motor-dependent stepping

to the correct location. The stage relaxes over the first 0.5 mm, during which irregular step sizes may result from loose contacts between drive and stage. One avoids this to first order by overshooting the beginning of the scan and tracking forward slowly and in uniform steps to the desired beginning. One minimizes it by measuring the position with the Heidenhain, and a third feature remeasures any count during which a significant (>0.5-μm) shift or relaxation has occurred. If the step width is not properly performed by the motor (as measured by the Heidenhain), a second attempt may be made, after which the program will halt if unsuccessful. A period of 0.5 s is allowed to elapse between counts so that there is sufficient time to step and to allow the stage to stabilize. A final correction for this lies in further analysis of profiles.

DEF is a double-emulsion film, but the nonnormal incidence angle of x rays makes it a source of double lines and conveys no further useful information; the densitometer will also focus on only one of the two emulsions, so all densitometry uses films with the reverse emulsion removed with 0.1 M of NaOH followed by cleaning with water. The sides and edges are taped to glass during this process so that an attack of the remaining emulsion by NaOH or water is avoided.[8,12] The emulsion (on the lower surface) is pressed flat on the stage and imaged on a viewing screen so that the grain structure can be observed. Traversing a 100-mm length shows minor loss of focus, but there is a small curvature of the film in a transverse direction. This will average the density over a slightly larger region than the 20-μm slit width, but the effect is small and introduces no significant shifts.

Before densitometry the exposed edge of each film was aligned to the longitudinal drive axis to better than 0.1 mm over 90 mm. This edge gave a good estimate of the central plane of the spectrometer.[11]

Variation of the illumination focus on the emulsion surface provides another source of imprecision. The illumination itself uses a stabilized power supply and a constant-current supply of 2–4 A to the source. This is measured as stable within statistics over hours of operation. The method for obtaining (uniform) photon statistics is discussed in CI, Section 5. This enables glitches (caused by power surges) to be eliminated when the counts in the first 0.5 s are compared with those in the remaining counting period and discrepancies outside two standard deviations are rejected.

4. Absolute and Relative Densitometry

Experimental densities relate to a background or unexposed region of the film with an offset added. Relative densities are reliable, but absolute density estimates are poor. Attempts to compare different films or scans with these estimates can involve discrepancies of density of 0.1 or more, unless calibration wedges are used. They are reliable relative density estimators over restricted ranges of D, but we are concerned with absolute densities and with densities varying from 0 to 4.

An improved method used the density of the most transparent channel as the zero estimate with a small offset for the fog level.[8] Evaluation of the minimum over a local (10-mm) scan of 500 channels can still yield significant variance.[11] Long automated scans with ~ 5000 channels reduce this scatter markedly and permit the remaining intensity variation to be meaningfully discussed. The current arrangement also established the zero as the minimum channel density of 9–20 parallel scans of a given film when basing observations at a common level.

Variations from the mean emulsion thickness occur, especially at edges and emulsion holes, or where cracks may develop.[13] They are significant only for high exposures and may give a slight shift to the background level or yield a glitch in our spectra, but they are otherwise insignificant. The definition of the minimum density as an average over three to five adjacent channels averages over most glitches (emulsion holes) and improves the estimate. Any scans of a different densitometer run (with a different initial zero setting) use this offset to yield a smooth and continuous background. Absolute densities are then reliably estimated, and relative densities and intensities within each film may be determined.

5. Allowance for Fog

Densities produced by densitometers are relative to some such zero level. In the equations in CI and CII they are compared with unexposed but developed emulsions. Hypersensitivity, fog, and background exposure need to be minimized or allowed for if the effects of (additional) monochromatic x-ray irradiation are to be considered. These effects may expose grains uniformly throughout the emulsion, preferentially at the surface or declining exponentially as a consequence of absorption. Allowance can be made by redefining the zero level, reducing the number of free grains per unit volume, identifying the background density D_b, and defining I (x rays) $= I(D) - I(D_b)$.

For an observed density D, an observed fog density D_{bf} at an unexposed region of the film, and a maximum density $D_{\max}$ obtainable with the given film and developer, the density caused by fog on an image is estimated[14] as

$$D_f = \frac{D_{\max} - D}{D_{\max}} D_{bf}. \tag{2}$$

Fog is less near high densities because available grains are reduced and soluble bromides generated during development restrain fog development. Equations (3), (4), (7), *et seq.* in CI could use $D - D_f$ instead of D, although variation in the fog level with position can invalidate this.[13]

Background fog levels from the sensitization of grains in DEF emulsion preparation in these conditions yield $D_{bf} \leq 0.12$. The variation in D_f with D is negligible for DEF emulsions, since $D_{\max} \gg 4$; thus

only a constant shift caused by fog is required. Aerial fogging, reticulation, and pressure marks are eliminated by a correct development and drying technique.

Dichroic fogging D_{df}, from the development of silver halides dissolved by developer solvent, is greatest in regions of maximum development. It should lie on the surface layer only (randomly distributed), so that a constant spatially varying density component may be added to the true density. This can give $D_{df} \rightarrow 0.5$, which could preclude further analysis in affected regions. Where D_{df} changes rapidly no analysis is sensible, but for regions where it is nearly constant the effects on centroids is random and may average to zero, while intensities of weak lines will be increased and distorted compared with stronger lines. For line images on emulsions, this kind of fogging is readily identified, and it is observed to be $D_{df} < 0.1$ in regions of interest.

D_{df} reduces the number of available grains (in the surface layer) without affecting absorption coefficients. Effective densities are slightly reduced for a given intensity, while errors are slightly greater. The background exposure on the film dominates the fog level in our case, and the effective increase in observed density should be < 0.12 for the most transparent background region and negligible for all peaks (and tails of peaks).

6. Reciprocity and Development

The intermittency effect, where a series of discrete exposures gives a larger or smaller effect than a continuous exposure with the same number of incident photons, is a manifestation of reciprocity law failure. The experimental technique uses a 30-Hz beam cycle, and these effects are important for visible and UV light. However, x rays give a chain reaction that tends to create a developable speck with a single photon, and hence both low- and high-intensity failures are evaded.

Solarization is connected with both exposure and development; it decreases density when exposure is increased at high exposure levels. Exposure is then a nonmonotonic two-valued function of density; thus linearization becomes impossible. Standard linearizations would show a symmetrical hollow at the center of strong peaks. Effects associated with varying densities along the emulsion (as with Lyman–Balmer peaks) include Eberhard and Kostinsky effects, where densities in, near, or between dense images are reduced by soluble bromides released during development. These effects are negligible for low densities, small for strong developers (hydroquinone) and longer development times, and reduced by background exposure or fog (Ref. 14, p. 875).

Following the recommended 5-min duration for D-19 developer implies that the density should have approached its limiting value by this time.[15–18] Evenness of developmental time is attained by use of a developing tank system with periodic agitation where the addition of each solution is completed within 10 s for typical film. No flattening, hollowing, or repulsion of peaks was observed with DEF emulsion, D-19 development, and standard conditions at densities up to $D = 4.0$.

Migration of grains during swelling, drying, and development can yield shifts of centroids and relative intensities. Silver clusters may be displaced by a grain diameter (with a maximum error of 1.6 μm, typically 0.6 μm in a random direction, with the mean error vanishing). Drying may introduce errors of 2 μm, especially if the base suffers from shrinkage effects, but this is mainly near the edge and in our case should be uniform along the film. Our films appear to be free from serious errors of those sorts.

7. Features of Experimental Data

The variation in density across and along the exposed portion of the films typically includes a smooth variation of peak location caused by the fast beam Doppler shift (and a broadening from angular divergence) and a smooth component along the film from scattered electrons and background radiation (Fig. 2). This variation dominates over the base fog level for most of the film. Superimposed on some films is a sharp feature caused by direct radiation from the source not prevented from reaching the film. This is dominant at the film edge closest to the source and is negligible in regions of importance. Sometimes a diffuse shadow or cloud which arises from dichroic fogging, is displayed over some portion of the film. Dichroic fog on some emulsions is serious with respect to relative intensities but occurs only near the secondary (third-order Lyman-α) lines; thus it does not show significant effects in this study. It does not occur in any Lyman-α–Balmer-β region.

8. Collimation and Errors

Contributions to uncertainties and variances from x-ray counting, grain counting, and densitometer photon-counting statistics, and experimental contributions from inadequate conversion to specular densities and allowance for background errors, were discussed in CI and CII. We assume that the current procedure gives negligible contributions to background uncertainty and intrinsic linearization formulas, so that statistical variance estimates provide uncertainties of linearized spectra.

A larger source of error concerning the photon intensity on the film relates to the collimating wires used for alignment. These occlude ~0.1 mm of the film for the length of the film and are roughly parallel with 1-mm spacing. The density observed normally includes a 10% transmission from these wires. In some scans two wires (or no wires) may occlude the region, giving rise to (spurious) intensity variation between scans.

We could correct for this problem on average by defining the area and number of available grains (M_0) to be reduced by 10%. Within the assumptions in Eqs. (3) and (4) of CI, this is equivalent to multiplying the density by 1/0.9 (to give a mean density for the exposed region) and scaling the incident x-ray count $I_p = I \times A_d$ by 0.9. (The estimate of the number of

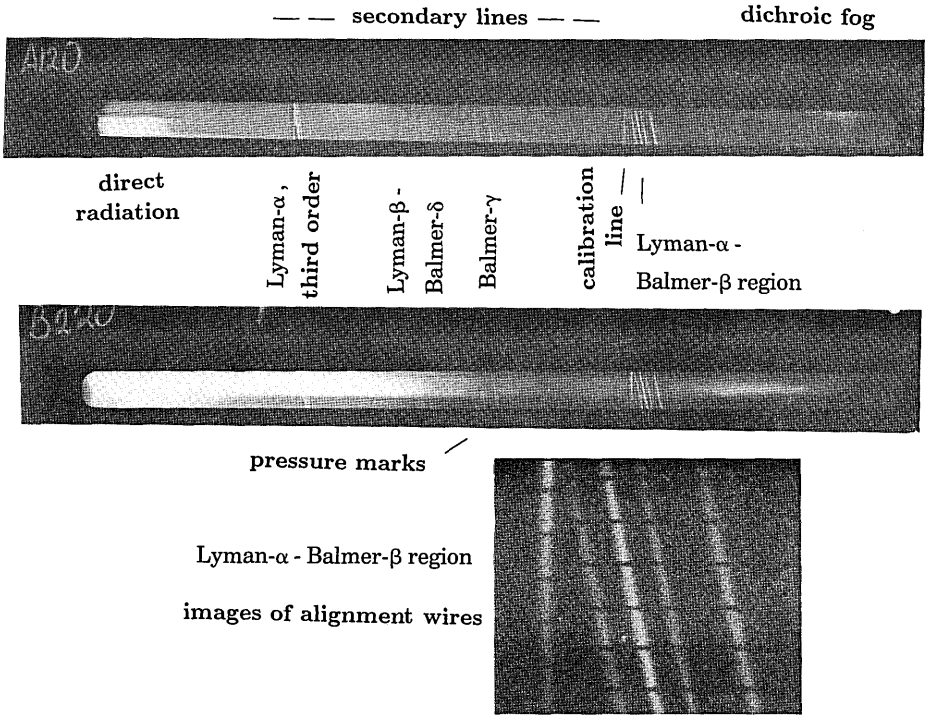

Fig. 2. Prints of a pair of typical films in the iron experiment, diffracted by PET crystals. The Lyman-α–Balmer-β region is expanded below; images of alignment wires for curved (Doppler-shifted) hydrogenic transitions, compared with those for stationary source calibration lines (in this case SiKα), are shown. The images are shifted since the sources are not coincident. Secondary lines, clearer in A120, are labeled. On the smooth background variation is superimposed strong exposure from direct radiation in the short-wavelength region (A120). Clamping (pressure) marks lie at the end of the film from the drying process and at the side edges resulting from the use of a tank system in the development. A120 shows two faint regions of (dichroic) fog; B220 appears to be seriously affected by this.

photons for the 20 × 1000 μm^2 region would not require scaling by 0.9, but error estimates should use the reduced value.) Variation from scan to scan would involve scaling densities by 1.00–1.20. This can shift intensities by a factor of 2. Within each scan, however, the error is constant; so it is not included in linearization or error estimates. They may be accounted for best by observation of relative x-ray counts for given peaks in different scans, with scaling that corrects for this. Symmetric distortion of channel intensities will occur for rapid changes in density, tending to make widths broader and the peaks of slightly more Gaussian character. (Tails will have a smaller shift to a Lorentzian character.) This typically represents a $<3\%$ increase of widths with up to a 26% shift of the (peak) profile character.

Errors of A_d have no effect on relative intensities within scans and do not distort noise or asymmetry; so they are not propagated to the peak fitting routine in the error field. They also do not affect calculations of x-ray production cross sections since the area factor cancels.

9. Effect of Angle on the Profile

In preceding equations we calculated the exposure for a region of uniform mean density with statistical fluctuations. Increasing exposure is assumed to darken deeper layers as viewed by the densitometer. However, spectral lines are of finite and narrow width and may show a large variation across the slit width in the densitometer; lines are curved or locally slanted with respect to the densitometer drive and rectangular slit region; and the emulsion is observed at normal incidence while irradiation takes place at angle θ.

Lyman (and Balmer) linewidths are of the order of 230 μm (full width at half-maximum). This is much larger than longitudinal step sizes and slit widths of 20 μm, a grain diameter of 1.6 μm, and graininess at densities of 0.3 of ~5–6 μm. If spectral lines were parallel to the slit, each peak would be divided into 11 or 12 sections: near an optimum division with regard to statistical noise. Peaks correspond to densities of ~2 (for example); so the channel with a maximum range of density is that at half-maximum, which may typically have a density of 0.5–1.2 with a variation of ~0.15–0.6 in density from one side of the slit to the other. These densities correspond to the end of the toe or the linear region of the $D - \ln I$ curve; so Eq. (33) of CI holds to some approximation:

$$D = -\log_{10}\tau \simeq C_3(\log_{10} z_{\max} + 0.5772) - C_4 z_{\min},$$

$$z_{\max} = \sigma\beta I.$$

The transmission, averaged by the densitometer, is then $\tau \simeq AI^{-C_3}$, $C_3 \simeq M_0 S(\sin\theta/\mu'\bar{d})$. Relevant energies, absorption, and scaling coefficients are given in Table 2 for the parameter values from CI and CII and for Lyman-α and Balmer-β energies of iron and germanium. Linearized exposures will be undis-

Table 2. Absorption and Scaling Factors for Lyman-α–Balmer-β Radiation, Fe^{25+} and Ge^{31+} [a]

	Charge State					
	Fe^{25+}		Fe^{25+}		Ge^{31+}	
Transition	Ba-β	Ly-α	Ba-β	Ly-α	Ba-β	Ly-α
E (keV)	1.7	7.0	1.7	7.0	2.8	10.6
Spectrometer, diffraction in first or fourth order						
Diffraction plane	PET 002	PET 008	ADP 101	ADP 404	Si 111	Si 444
θ^R	0.955	0.955	0.734	0.734	0.842	0.842
μ_0	0.099	0.0015	0.099	0.0015	0.0232	0.00044
μ_1	2.192	0.148	2.192	0.148	0.636	0.050
μ'	0.50	0.057	0.48	0.057	0.22	0.020
$\frac{z_{max}}{z_{min}} = \exp(-\mu' T/\sin\theta)$	3.5^{-4}	4.0^{-1}	9.0^{-5}	3.3^{-1}	2.2^{-2}	7.1^{-1}
C_3 (Section 9)	1.0	8.2	0.9	7.4	2.1	23.5

[a] $\bar{d} = 1.6$ μm, $T = 13.0$ μm, $M_0S \simeq 0.94$; the exponential notation is an abbreviation and should read in full as ×10 to the power indicated.

torted for Balmer radiation. Averages of I^{-8}, I^{-24} over ranges of ±7.5% and ±3.0% for Lyman radiation decrease mean intensities by only 0.9% and 0.3% for iron and germanium data, respectively. The variation of exposure in the densitized region for this particular agreement would not yield a major systematic correction.

Lines are slanted because of the Doppler shift, and although it is possible to scan normal to the local curvature over a short range of the film, the result is difficult to analyze. The mean angle to the spectrometer plane is 12.25 ± 0.1° with the lower edge typically 11.2° and the upper edge 13.4° because of the curvature of the lines. The angle of the spectrometer plane to the slit is $\alpha'' \simeq 0.285°$, so that the densitized region lies at 10.9–13.1° to the line curvature. The variation in density is then dominated by that from the top to the bottom of the slit. This will cross the peak, lowering (peak) densities substantially. The average density is a relatively reliable measure of the mean exposure, as indicated by the I^{-8} averages above.

The most serious effect will be on the linewidths, which are broadened by this convolution with the slit function. For 1-mm heights Lyman and Balmer widths increase because of this 200-μm broadening by from 30% to 100%. These estimates are uncertain because of the alignment wires and other effects.[11] Conversely, densitometry with a slit height of 0.4 mm gave negligible shifts of centroids or intensities, while the slit broadening was reduced to 89–107 μm. The narrow height increases individual scan variance, but the convolution problem is nearly eliminated, and the greater number of scans gives improved estimates of spectrometer parameters and reduced final uncertainty. This is a way of dealing with some of the more dominant effects of slanted lines and rectangular densitometry. A comparison of results with narrow and wide slit heights confirms spectral resolution and intensities and gives information on deconvolved profiles.

The photon incidence angle on the emulsion is fundamental and alters both the centroid determination and the linearization formula. For a narrow beam of x rays incident at an angle of ≃56° (the iron Lyman–Balmer region using PET crystals), the region of emulsion exposed in the first monolayer is displaced around the film from the region in the last layer of emulsion. This is different for varying energies and angles. Iron Lyman radiation (assuming negligible absorption) may give a mean shift of the observed line by up to $(T \tan\theta)/2 \simeq 9.6$ μm compared with a negligible shift for weakly penetrating Balmer radiation. The shift is nearly half of a channel width, so must be accounted for. It is simple to include a centroid correction in profile analysis[11] by using the mean attenuation coefficient. The profile will include a skew component of up to 9.6 μm in width convolved with the profile at the surface of the emulsion, which is also readily included in profile analysis or deconvolution.

The more fundamental effect on intensities of irradiation at angle θ with densitometry at normal incidence is discussed in part in CII, Section 5. The complexities of this model will require explicit evaluation of the angular dependence (under the given assumptions) for a range of energies and angles. This is not pursued in this paper. However, the major ideal, broad-source dependence follows that explained in CI, Section 19.

This discussion assumed that any narrow photon flux was incident normally, so that the density at a given point corresponds to transmission of the same incident light through that section of film; whereas the density at one section will be solely due to the exposure of the surface monolayer, while that at the section 9 μm along will be due only to exposure of the deepest layer. Fortunately unconvolved widths are at least six channels (115 μm) so that any 20-μm slit width experiences the same incident flux across this 4–9-μm length. In other experimental arrangements this issue must be reassessed.

10. Comparison of Linearizations

An important difficulty in linearization of Lyman–Balmer regions arises from the overlap of different

orders and energies. In Fig. 3 we emphasize this by showing spectral profiles in the Lyman-α–Balmer-β region for particular scans of three different DEF films, one for iron spectra diffracted with a PET crystal, one diffracted with an ADP crystal, and one for germanium spectra diffracted with a silicon crystal. They illustrate the effects of large ranges in density of 1.2, 3.0, and 2.8, respectively. Circles with bars indicate the best estimates of absolute incident photon counts with total statistical (grain, x-ray, and

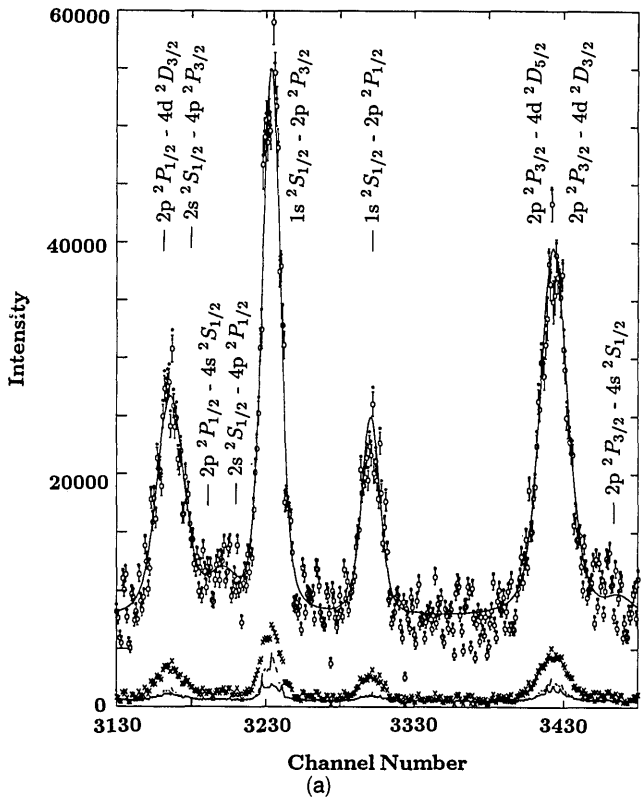

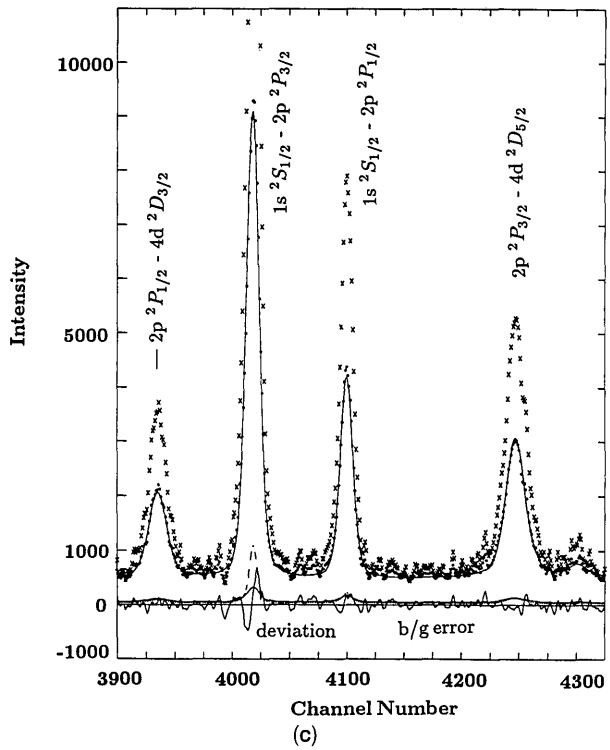

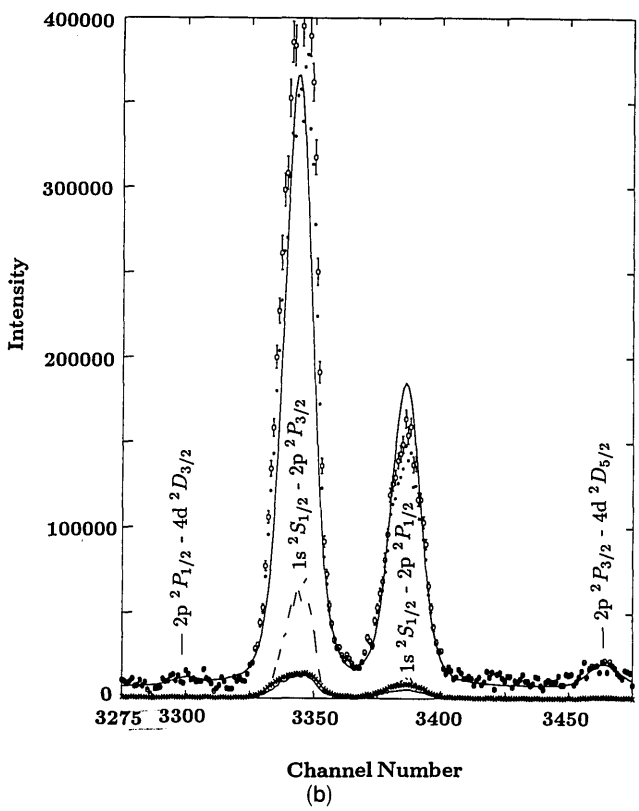

Fig. 3. Comparison of linearizations and errors for Lyman-α (1*s*–2*p*)–Balmer-β (21–41′) spectral regions with resultant fits with Voigt profiles. Linearizations of Ref. 11 (*) with error field (---) are compared with typical fits (—), with linearizations of model 6 of CII (○ with error bars, and error field —) when first-order (Balmer) energies are assumed, and with corresponding linearizations (×) when fourth-order (Lyman) radiation is assumed.

Intensities (photons per channel with a typical height of 0.4 mm and width of 20 μm) are plotted against channel number. (a) Linearization A120T of exposure A120, scan 1, for PET diffraction of Fe^{25+} radiation. (b) Linearization A317A of exposure A317, scan 2, for ADP diffraction of Fe^{25+} radiation. (c) Linearization BX25A of exposure X25A, scan 6, for silicon diffraction of Ge^{31+} radiation. Model 6 linearization is similar to that of Ref. 11; thus it is omitted for clarity, while we include the discrepancy of fits (—) to compare with error fields. The b/g error is indicated by the deviations between well-separated peaks, far from profile tails.

detector sources) uncertainties, following CII and model 6. Stars indicate a similar model, described in detail in Ref. 11, fitted by use of a smaller data set and with minor modifications below, with the (dashed) error field repeated as the solid curve near the zero level. This indicates variation resulting from modeling.

These linearizations agree at estimated one- or two-standard-deviation levels, although quoted intensity error estimates differ significantly. Contributions from detector statistics are unchanged. The earlier model underestimated the background (low-D) uncertainty from x-ray statistics by considering only N_{inc} (CI, Section 3 and CII, Section 7) and overestimated high-D uncertainty with a different form of correlation parameters and grain uncertainty. In the three examples plotted the uncertainty for D = 0.1 was underestimated by 22%, 45%, and 47%, respectively; that for D = 0.5 was overestimated by 12%, −8%, −13%; and that for D = 1.3 was overestimated by a factor of 2.3, 1.7, 1.7 for the three Lyman-α–Balmer-β regions. For peak densities on the latter two films (D = 2.75, D = 3.05) this overestimation reached factors of 5.2 and 4.1.

These factors lead to different χ_r^2 values for fits but with similar areas and profiles. The scatter in Fig. 3(a) is typically twice the error field, which suggests that the smooth background is not dominated by low-energy photons as linearized but by electrons or higher-energy x rays. Asymmetry is distorted slightly, but symmetric profiles have undistorted centroids. The χ^2 values are dominated by the inadequacy of fitting complex profiles with simple Voigt functions, which are compounded by the inadequacy of the first-order linearization for Lyman-α peaks. Figure 3(b) provides an extreme case of this, where the profiles are poorly fitted because of peak distortion. In such cases one may prefer to linearize, assuming fourth-order (higher-energy) radiation, and to correct Balmer radiation after fitting the profiles. Despite equally high densities, the precise fitting of profiles in Fig. 3(c) is achieved with deviations in agreement with error estimates, which indicates that radiation in this energy range may be responsible for the background levels observed. The experimental agreement of iron spectral relative intensities[11] from different films and after diffraction by PET or ADP crystals lies at the 25% level, which is the same order as experimental fitting uncertainties and provides some confirmation of the linearization and analysis procedure.

Lyman-α intensities incident on the film are much weaker for the iron data with PET diffraction, about the same for ADP diffraction, and much stronger for the germanium data with silicon diffraction. This follows from source strengths and diffraction efficiencies. Experimental ratios may thus be used for testing models for reflectivity from curved crystals.[19] The linearization for fourth-order-versus first-order radiation reveals an optimum sensitivity for DEF emulsion of ~7 keV and confirms the difficulty of fitting overlapping profiles with different energies and photographic sensitivities.

From Eq. (6) of CI we can estimate standard photon fluxes, from which the more exact but not readily invertible formulas of CII may be compared, by using tabular interpolation. The parameters from Ref. 15 with the assumptions therein were not plotted in the figures. Discrepancies between this and the current plots are −42%, −17%, −39% for D = 0.1; −25%, +5%, −28% for D = 0.5; −9%, +23%, −14% for D = 1.3; and +68%, +23% for the peaks of the latter films. This indicates the different effect of angle on the linearization between the method of Ref. 15 and that of CII. The lower χ_r^2 for the current model suggests that these discrepancies are inadequacies of the simpler model, particularly for densities below two, which will lead to errors of relative intensities if used. The simpler model is much better than linear or exponential assumptions for linearization, which have been used previously.[8,12] Relative Balmer-β intensities given by Henke's formulas appear to be accurate to a factor of 2, compared with the current model, but larger errors arise at angles that are far from normal incidence or at low energies.

11. Order Overlap

The energy and angle dependence of linearization along the film is slow but becomes important over the 100-mm lengths scanned in these experiments. Linearization must in any case make an assumption about the order of the dominant irradiation or the fraction of each kind at any given point. This assumption varies the expected x-ray energy by a factor of 4. The procedure adopted in the analysis of current experimental data is to initially linearize by assuming first-order radiation, which yields accurate values for the Balmer series and calibration source lines. Background exposure from scattered electrons from the beam and from direct or scattered light reaching the emulsion has a complex energy distribution but is smooth, is of low density in regions of interest, and may be neglected. Incorrect linearization of the Lyman series and heliumlike spectra must be considered. This arises from the variation of E and hence μ', μ_0, and μ_1 (absorption coefficients, see CI) for the same angle, focused onto the film in a different order of diffraction for a given crystal.

Linearized peaks are fitted in a self-consistent way throughout scans of a given film so that correlation is minimized. The resulting Lyman intensities or areas must then be corrected for the amount by which they have been overestimated in the linearization. We may use Eq. (6) of CI to estimate correction factors of this sort, particularly for relative intensity ratios within a given order. They confirm the trends and relative corrections in the table. It is less precise for comparing radiation from different orders and greatly differing densities. In Table 3 we present comparisons of correction factors using Eq. (6) compared with those using model 6 of CII for the range of window materials and thicknesses and main primary

Table 3. Linearization Correction Factors I(Lyman)/I(First Order)

Fe Radiation, PET Diffraction	Window (Section 11)				
	A1				B4
Transition	3Ly-α	4Ly-γ	4Ly-β	4Ly-α	4Ly-α
E (keV)	6.97	8.70	8.25	6.97	6.97
E (linearized)	2.32	2.175	2.063	1.743	1.743
θ^R	0.657	0.711	0.759	0.955	0.955
D = 0 Eq. (6), CI	0.359	0.424	0.349	0.157	0.155
D = 1 Eq. (6), CI	0.286	0.328	0.268	0.123	0.120
D = 2 Eq. (6), CI	0.221	0.250	0.198	0.0938	0.0907
D = 0.0	0.350	0.402	0.333	0.1618	0.1592
D = 0.5	0.350	0.402	0.327	0.1628	0.1585
D = 1.0	0.316	0.359	0.294	0.1447	0.1411
D = 1.5	0.290	0.324	0.261	0.1294	0.1264
D = 2.0	0.250	0.277	0.220	0.1090	0.1060
D = 2.5	0.215	0.233	0.179	0.0884	0.0861
	Be				None
D = 0 Eq. (6), CI	0.828	1.120	1.010	0.679	0.937
D = 0.00	0.808	1.057	0.966	0.697	0.965
D = 0.25	0.816	1.058	0.958	0.701	0.968
D = 0.50	0.812	1.056	0.953	0.696	0.964
D = 0.75	0.793	1.034	0.929	0.682	0.938
D = 1.00	0.734	0.955	0.853	0.620	0.857
D = 1.50	0.669	0.851	0.757	0.555	0.766
Fe Radiation, ADP Diffraction		A1			
θ^R		0.525	0.565	0.600	0.734
D = 0 Eq. (6), CI		0.261	0.278	0.228	0.0956
D = 1 Eq. (6), CI		0.201	0.202	0.158	0.0670
D = 2 Eq. (6), CI		0.136	0.141	0.106	0.0455
D = 0.0		0.251	0.259	0.216	0.0958
D = 0.5		0.244	0.256	0.206	0.0923
D = 1.0		0.211	0.217	0.177	0.0782
D = 1.5		0.184	0.187	0.147	0.0646
D = 2.0		0.151	0.150	0.114	0.0493
D = 2.5		0.121	0.118	0.0886	0.0362
D = 3.0		0.101	0.0882	0.0648	0.0233
D = 3.5		0.0756	0.0647	0.0454	0.0164

and secondary spectral regions for hydrogenic iron experiments. In Table 4 we give corresponding results for the hydrogenic germanium experiment.

This shows that linearity of photographic response fails at $\sim D = 0.5$ and quantifies the distortion of profiles by first-order linearization. It also indicates differing correction factors for strong and weak lines but shows that additional background density is of minor effect in this context. In most films from iron experiments, first-order linearization overestimates Lyman contributions for tails and more so for peaks. Peaks will appear narrower than they should be.

For PET diffusion at angles corresponding to Lyman-α, 83.7% of first-order radiation is absorbed by window A1 (334-nm aluminum coating on 50.8-μm polypropylene), while negligible (2.7%) fourth-order (Lyman) radiation is absorbed. Differential window absorption between windows A1 through B4 (with different, measured aluminum thicknesses) is 1–2%.

Table 4. Linearization Correction Factors I(Lyman)/I(First Order)

Ge Radiation, Si Diffraction	Window			
	Be			
E (keV)	10.6	13.24	12.55	10.6
E (linearized)	3.533	3.31	3.138	2.65
θ^R	0.594	0.640	0.681	0.842
D = 0, Eq. (6), CI	2.02	3.48	3.13	2.29
D = 1, Eq. (6), CI	1.63	3.21	2.88	2.02
D = 2, Eq. (6), CI	1.32	2.91	2.58	1.75
D = 0.0	1.809	2.661	2.470	1.981
D = 0.5	1.807	2.664	2.492	1.974
D = 1.0	1.683	2.664	2.483	1.962
D = 1.5	1.535	2.566	2.394	1.826
D = 2.0	1.400	2.502	2.298	1.756
D = 2.5	1.228	2.425	2.222	1.618

Use of 12.7-μm beryllium windows reduces the former loss to 28%, and changing the angle to that for ADP diffraction increases the loss to 91.5%. Thus window absorption dominates iron data corrections, while germanium corrections are dominated by transmission factors of radiation through the depth of the emulsion.

For the A120 film densitized with 1-mm slit heights (A120M), the strongest Lyman component gave a density maximum of 0.55–1.1 (which varied between scans because of the source distribution and alignment wires), the strongest Balmer component gave densities of 0.7–0.85 at the peak, and Lyman-α_2 gave a peak density of $\sim$0.22–0.55. Correction factors for particular peaks depend primarily on the density for the half-maximum intensity value (i.e., at the full width at half-maximum). This mean density is $\sim D_M = 0.5(D_{pk} + D_{b/g})$ for $D_{pk} < 1.4$ or $D_M \simeq D_{pk} - (0.6 \rightarrow 0.9)$ for higher densities. Typical values for the different films used in our experiments are illustrated in Table 5 for the fourth-order Lyman-α components. The Lyman-α_1 ($1s$–$2p_{3/2}$) component in A120M with densities at half-maximum of 0.65 or 0.3 for the strongest and weakest scans may be compared with that for Lyman-α_2 of 0.275 or 0.1. $[I(\mathrm{Ly}\alpha_1)/I(\mathrm{Ly}\alpha_2)]$ is then overestimated by 4%. For A317A, it is overestimated by 48%.

Table 5. Peak 1 (First-Order), D_{pk} and D_M Estimates for Typical Films

	Film						
	A120M	A120T	BX11A	A317A	B417A	A322S	BX25A
Crystal	PET	PET	PET	ADP	ADP	ADP	Si
Window	A1	A1	Be	A3	B4	A3	Be
Source	Fe	Fe	Fe	Fe	Fe	Fe	Ge
I(4Ly-α_1)	125k	52k	10k	640k	450k	200k	18k
D_{pk}	1.1	2.0	1.1	3.77	3.36	2.0	3.0
D_M	0.65	1.3	0.65	2.9	2.41	1.4	1.8
I(4Ly-α_2)	60k	19k	5k	280k	176k	110k	10k
D_{pk}	0.55	1.1	0.6	2.8	2.07	1.32	2.0
D_M	0.28	0.70	0.35	2.0	1.35	0.9	1.2

The accuracy of these intensity corrections is at the 2% level. Tabulated corrections have significant uncertainties where Doppler shifts cause the transition to cross a first- or higher-order absorption edge. The variation with energy is then discontinuous. There is a discontinuity in first-order iron radiation at 1.78 keV caused by Br L1. The interpolation of correction factors should be made from either side of the tables. The Br K edge affects germanium Lyman-γ/δ radiation; thus extrapolation from the table to higher energies is not reliable. Germanium Lyman-δ may show profile discontinuity in some scans as a result.

12. Densitometry Corrections

First-order linearization allows for most effects within the quoted output uncertainty. In this section we summarize those systematic and random error sources that are not so included.

(a) Scans containing alignment wires should be scaled up in intensity to those lines of adjacent scans (so that we can estimate photon fluxes and distribution). These scans are weak and may show large variances of centroids compared with adjacent scans because of reduced statistics or the nonparallelism of the wires with the drive. Such scans are given low weighting in the overall fits. Widths are normally smaller, but if the wire image is centered on the scan, a flat-topped or double peak may result.

First and last scans may cover part of the unexposed region and may be abnormally weak. If the spectrometer plane is poorly aligned, some peaks (usually third-order lines) may be absent from the first or last scans. Uncertainty in the area observed by the densitometer is at the 5–10% level but has a negligible effect on intensities (per unit area).

(b) Background electron scattering on the high-energy end of the film, and the effects of fogging that usually arise in the same region (a consequence of developing imprecision), has no effect at first order. Where this varies rapidly or quadratically, fogging may prevent weak lines from being fitted or measured to better than 40 μm or more, and fits are given appropriate uncertainty.

(c) Slanted lines yield average densities convolved with a slit function. They generally make lines easier to fit but decrease resolution. Areas and centroids remain constant, and heights of 0.4 mm minimize this.

(d) Linearization depends on energy; so energies and angles for two channels must be given initially. Several films have calibration lines for this purpose, but in other films corresponding channels may need to be specified *a posteriori* by comparison with Lyman or Balmer lines, which requires a test linearization first. Lyman and Balmer lines are Doppler shifted and appear slanted; so identification of these channels with particular energies yields an error. An error of 560 channels (which is 10-fold larger than a typical error from this source) gives intensity errors at the 1% level, because linearization is a slow function of angle and energy.

(e) The linearization here uses a double interpolation for intensity versus density, between D and between two energies/angles, beyond the extremes given in Table 3. The D interpolation is accurate to 1%, especially at low densities. It may be compared with first-order shifts for PET iron data from values following Ref. 8 by, e.g., 30% at low densities to 9% at $D = 1$, 8% at $D = 2$, and 12% at $D = 2.5$.

However, E interpolation overestimates intensities at intermediate energies by up to 14% with relative intensities that are accurate to 3%. Absolute intensities in the Lyman-α–Balmer-β region are typically accurate to 4% (with a relative intensity accuracy of 1%). This may be corrected for by scaling Lyman-α–Balmer-β intensities by 0.96, Balmer-γ by 0.86, Lyman-β–Balmer-δ by 0.9, Balmer-ϵ by 0.95, and third-order Lyman-α intensities by 0.99. At important regions (Lyman-α) these shifts are the same size as the uncertainty (1–3%).

(f) Error estimates for each channel use the same interpolation method. This underestimates errors for densities by up to 10% for intermediate angles. For densities over 0.2 (i.e., where lines exist) this has a relative error of 2–3%. This increases χ^2 of fits slightly but has a negligible effect on parameters.

(g) Corrections of relative intensities for order overlap in iron spectra with PET diffraction are given in Section 11 and dominate most other effects.

(h) The *fits* of linearized profiles may underestimate or overestimate the peak areas because of the differences between fitting and linearized profiles, low background errors, or statistics. An example is provided by fourth-order Lyman-α radiation diffracted from ADP crystals over long exposures [Fig. 3(b)]. These are very strong ($D \simeq 3.7$) lines with weak Balmer lines nearby. The effect of linearization errors (g) is to increase tails by factors of 10 and peak intensities by factors of 60! Low background and large peak errors force the fit to underestimate the peak height and area by 25–29% for strong Lyman-α_1 peaks (films A317A, B417A). B422S and A322S have a 10–15% error from this source. Lyman-α_2 components are affected at the 1–8% level, which is at the level of the fitting uncertainty. No other lines of films need this correction.

Lyman radiation diffracted in third order may be strongly asymmetric in profile for germanium data[19] but is fitted with symmetric functions. These lines are strong, and intensities may be underestimated by 20–25%. Centroids may also need correction, if these peaks are used in a subsequent analysis.

(i) To gain relative or absolute intensities produced by the source, results are scaled by integrated reflectivities of the diffracting crystal. The observed component of the film is usually π-polarized; thus scaling gives the π component of absolute source intensities and a 50% estimate of the total. This

estimate can be improved with detailed investigations.[11]

Potential centroid errors include asymmetric depth penetration for nonnormal incident angles, smaller shifts of <0.2 μm for any channel because of grain extrusion and migration from adjacent channels, 1.0 μm for any channel from the Heidenhain reading error, stage relaxation and the drive periodicity, ~ 10 μm/60 mm for a linear thermal drift, and ~ 20–40-μm shift from one scan to the next. The total position uncertainty is dominated by the effects of profile asymmetry, diffraction shifts, and other systematics.[11]

13. Conclusions

We have inverted the models from previous papers and applied them to specific experiments and densitometry procedures, and we have discussed the effects and corrections relevant in the derivation of centroids, profile widths, assymmetry, and areas, allowing an accurate estimation of relative and absolute intensities and profile widths with statistical uncertainties.

These procedures may be applied to other energies, emulsions, and spectrometers, as noted in CII for Kodak 101-07. The optimized correlated model used here appears to be more reliable for extension to other densities, angles, and energies than earlier models, but further photographic experiments, particularly at high densities, varying angles and ranges of energy, appear to be necessary for further investigation of these findings.

The authors thank Shell Australia, the Hasselblad Foundation, and the Draper's Company for support of this research and St. Anne's College, Oxford, for a Junior Research Fellowship covering part of the period of research. This work was partially supported under the auspices of the U.S. Department of Energy by the Lawrence Livermore National Laboratory under contract W-7405-ENG-48. Acknowledgments go to J. M. Laming, W. A. Hallett, and J. S. Brown for assistance and support and also to A. J. Varney for helpful comments.

References

1. C. T. Chantler, "Photographic response to x-ray irradiation I: estimation of the photographic error statistic and development of analytic density-intensity equations," Appl. Opt. **32,** 2371–2397 (1991).
2. C. T. Chantler, "Photographic response to x-ray irradiation II: correlated models," Appl. Opt. **32,** 2398–2410 (1992).
3. C. J. Hailey, R. E. Stewart, G. A. Chandler, D. D. Dietrich, and R. J. Fortner, "A precision measurement of the $^2P_{3/2}$–$^2P_{1/2}$ fine-structure splitting in hydrogenic iron and zinc using beam-foil spectroscopy," J. Phys. B **18,** 1443–1448 (1985).
4. D. D. Dietrich, G. A. Chandler, R. J. Fortner, C. J. Hailey, and R. E. Stewart, "Observation of electric quadrupole decay in Xe^{45+} and Xe^{44+}," Phys. Rev. Lett. **54,** 1008–1011 (1985).
5. D. D. Dietrich, G. A. Chandler, R. J. Fortner, C. J. Hailey, and R. E. Stewart, "Precision x-ray spectroscopy on 8.5MeV/amu heavy ions," Nucl. Instrum. Methods B **9,** 686–688 (1985).
6. J. D. Silver, A. F. McClelland, J. M. Laming, S. D. Rosner, G. C. Chandler, D. D. Dietrich, and P. O. Egan, "Simultaneous observation of Lyman-α and Balmer-β transitions in hydrogenic iron, Fe^{25+}: a novel technique for 1*s* Lamb-shift measurement," Phys. Rev. A **36,** 1515–1518 (1987).
7. J. M. Laming, C. T. Chantler, J. D. Silver, D. D. Dietrich, E. C. Finch, P. H. Mokler, and S. D. Rosner, "A differential measurement of the ground state Lamb shift in hydrogenic germanium, Ge^{31+}," Nucl. Instrum. Methods B **31,** 21–23 (1988).
8. J. M. Laming, "A differential measurement of the ground state Lamb shift in hydrogenic germanium, Ge^{31+}," D.Phil. thesis (University of Oxford, Oxford, 1988).
9. W. A. Hallett, "Measurement of $\Delta n = 0$ transitions in helium-like neon and silicon," D.Phil. thesis (University of Oxford, Oxford, 1991).
10. J. S. Brown, C. W. Band, E. C. Finch, R. A. Holt, H. A. Klein, J. Laursen, A. F. McClelland, N. J. Peacock, J. D. Silver, M. F. Stamp, and J. Takacs, "Studies of 1*s*2*s* ^3S–1*s*2*p* ^3P transitions in helium-like Ne^{8+} recoil ions using photographic spectroscopy," Nucl. Instrum. Methods B **9,** 682–685 (1985).
11. C. T. Chantler, "Beam-foil spectroscopy of highly-ionized atoms, precision measurements of hydrogenic Lamb shifts and x-ray diffraction of curved crystals," D.Phil. thesis (University of Oxford, Oxford, 1990).
12. A. F. McClelland, "Development of a novel technique for the measurement of the $1s_{1/2}$ Lamb shift in high Z hydrogenic ions by Lyman α/Balmer β wavelength intercomparison," D.Phil. thesis (University of Oxford, Oxford, 1989).
13. G. M. B. Dobson, I. O. Griffith, and D. N. Harrison, *Photographic Photometry* (Oxford U. Press, London, 1926).
14. C. E. K. Mees, *The Theory of the Photographic Process* (Macmillan, New York, 1946).
15. B. L. Henke, J. Y. Uejio, G. F. Stone, C. H. Dittmore, and F. G. Fujiwara, "High-energy x-ray response of photographic films: models and measurement," J. Opt. Soc. Am. B **3,** 1540–1550 (1986).
16. P. D. Rockett, C. R. Bird, C. J. Hailey, D. Sullivan, D. B. Brown, and P. G. Burkhalter, "X-ray calibration of Kodak direct exposure film," Appl. Opt. **24,** 2536–2542 (1985).
17. W. C. Phillips and G. N. Phillips, Jr., "Two new x-ray films: conditions for optimum development and calibration of response," J. Appl. Crystallogr. **18,** 3–7 (1985).
18. B. L. Henke, S. L. Kwok, J. Y. Uejio, H. T. Yamada, and G. C. Young, "Low-energy x-ray response of photographic films. I. mathematical models," J. Opt. Soc. Am. B **1,** 818–827 (1984).
19. C. T. Chantler, "X-ray diffraction of bent crystals in Bragg geometry I: perfect crystal modelling," J. Appl. Crystallogr. **25,** 674–693 (1992).